Surfaces and Interfaces 80 (2026) 108318

Contents lists available at ScienceDirect

Surfaces and Interfaces

journal homepage: www.sciencedirect.com/journal/surfaces-and-interfaces

Tunable gas sensing properties of metal-doped C_3N for agricultural molecule detection: A DFT study

Watcharin Teeranattapong, Audomsak Sripothongnack, Thanasee Thanasarnsurapong, Chatchawal Wongchoosuk, Pakpoom Reunchan *

Department of Physics, Faculty of Science, Kasetsart University, Bangkok 10900, Thailand

ARTICLE INFO

Keywords:
C_3N
Doping
Aldehyde
Gas sensor
DFT

ABSTRACT

Developing advanced gas sensors is crucial for modern agriculture, where the early detection of stress-indicating gases is vital for effective crop management. Two-dimensional (2D) materials, with their high surface-to-volume ratio and tunable electronic properties, offer promising sensing capabilities. In this work, we employed density functional theory (DFT) to investigate the adsorption behavior and sensing potential of C_3N monolayers toward four gas molecules, H_2O, CO_2, C_2H_4, and C6-aldehyde. We considered both pristine C_3N and variants doped with Na, Mg, and Al atoms at vacancy sites. Our results show that Al-doped C_3N exhibits the strongest interaction with CO_2, C_2H_4, and C6-aldehyde, while Mg-doped C_3N demonstrates moderate binding, especially with H_2O. Na-doped C_3N shows the weakest adsorption. Bader charge analysis reveals distinct charge transfer behaviors depending on the dopant and adsorbate. Additionally, recovery time calculations indicate that metal doping significantly enhances the gas-sensing performance, particularly in Al- and Mg-doped systems. These findings offer insights into the rational design of high-performance C_3N-based gas sensors suitable for agricultural applications.

1. Introduction

In modern agriculture, early detection of plant-emitted chemical signals is essential for monitoring crop health and mitigating the effects of environmental stress [1,2]. When exposed to abiotic stressors such as drought, heat, or pathogen invasion, plants emit various volatile and semi-volatile molecules—such as carbon dioxide (CO_2), ethylene (C_2H_4), water vapor (H_2O), and aldehydes (e.g., C6-aldehyde)—that serve as chemical biomarkers of physiological stress responses [3,4]. These molecular emissions often precede visible symptoms, making them valuable targets for real-time sensing. To capture these signals reliably, gas sensors must exhibit high sensitivity, fast response and recovery, selectivity, and stable operation under ambient environmental conditions [5,6].

Two-dimensional (2D) materials have emerged as promising candidates for gas sensing due to their large surface area, tunable electronic properties, and high surface reactivity [7,8]. In particular, carbon-based 2D materials such as graphene [9–11], graphyne [12,13], graphdiyne [14], nitrogen-doped derivatives [11,15–17], and other emerging 2D materials have attracted considerable interest [18,19]. These materials demonstrate excellent electrical conductivity, mechanical strength, and structural stability, making them suitable for sensor applications. Graphene, for example, was first shown as a gas sensor for NO_2, with detection limits as low as 1 part per billion [9]. Since then, numerous studies have explored both pristine and functionalized graphene for sensing various analytes. However, pristine graphene has limited sensitivity to some non-polar gases due to its low reactivity [20]. To overcome this, strategies such as defect engineering, heteroatom doping (e.g., N, B, or O), and surface functionalization have been explored. Nitrogen-doped graphene and its derivatives have shown enhanced gas adsorption characteristics and improved sensitivity. Beyond graphene, other heteroatom-rich carbon-nitride frameworks, such as C_2N and BNC_2, have attracted significant attention for gas sensing due to their tunable electronic properties and high chemical reactivity. For instance, first-principles studies have demonstrated that C_2N monolayers exhibit strong adsorption and charge transfer with molecules such as NO_2 and NH_3, making them excellent candidates for sensors [21,22]. In addition, BNC_2—a boron–nitrogen–carbon hybrid sheet—has been extensively explored. DFT work highlights its high selectivity toward gases such as CO, CO_2, NO, and NO_2, and demonstrates how metal dopants (e.g., Al)

* Corresponding author.
E-mail address: pakpoom.r@ku.ac.th (P. Reunchan).

https://doi.org/10.1016/j.surfin.2025.108318
Received 13 October 2025; Received in revised form 10 December 2025; Accepted 11 December 2025
Available online 12 December 2025

can further enhance adsorption and sensor performance [23,24].

More recently, C_3N has emerged as a promising carbon–nitride 2D material [25]. It features a graphene-like structure with periodic nitrogen substitution, conferring higher chemical activity and tunable electronic properties [26]. Mahmood *et al.* first synthesized C_3N experimentally via pyrolysis of hexaaminobenzene (HAB) trihydrochloride single crystals [27], revealing a thermally stable semiconducting monolayer verified by STM/STS characterization. Subsequent experimental and theoretical studies have examined C_3N for electronics, energy storage, and gas sensing. For example, recent DFT studies show NO_2 adsorption on C_3N, confirming strong adsorption capacity and sensing potential [3,28]. Similar DFT studies have also reported strong sensitivity of C_3N toward NO and other toxic gases [10,11].

Despite these advances, the potential of C_3N for detecting agriculturally relevant gases, such as H_2O, CO_2, C_2H_4, and C6-aldehyde, remains largely unexplored. Furthermore, metal doping has been proposed as a viable strategy to enhance gas adsorption by modifying the electronic structure and increasing the number of active sites.

In this work, we systematically investigate the adsorption and sensing behavior of pristine and metal-doped C_3N monolayers using van der Waals-corrected density functional theory (DFT). Three dopants, Na, Mg, and Al, are examined. Na, Mg, and Al were chosen to represent alkali, alkaline-earth, and post-transition metals, respectively. Their different atomic radii and electronegativities allow systematic adjustment of charge transfer and bonding strength on the C_3N surface. These lightweight, inexpensive dopants can be stably incorporated into vacancy sites without causing significant lattice distortion. Additionally, previous DFT studies reported that Al-doped C_3N shows a notably stronger interaction with CO and a significant reduction in band gap, confirming its excellent potential for gas sensing [29]. We evaluate adsorption energies, charge transfer, electronic structure modifications, and work-function changes to assess recovery time and sensing sensitivity. Our results reveal that metal doping, particularly with Al and Mg, substantially enhances the interaction with target gases, underscoring the promise of C_3N-based monolayers as highly sensitive and selective gas sensors for agricultural applications.

2. Computational method

First-principles calculations were performed using the Vienna Ab initio Simulation Package (VASP) [30,31]. The interactions between core and valence electrons were described using the projector augmented-wave (PAW) method [32]. The exchange–correlation functional was treated within the generalized gradient approximation (GGA) using the Perdew–Burke–Ernzerhof (PBE) scheme [33]. A plane-wave cutoff energy of 520 eV was employed. For Brillouin zone integration, a Monkhorst-Pack *k*-point mesh of $9 \times 9 \times 1$ was used for the primitive cell [34].

To investigate the interaction of gas molecules on pure and doped C_3N, we adopted a $3 \times 3 \times 1$ supercell of C_3N, comprising 54 carbon atoms and 18 nitrogen atoms. A vacuum space of 30 Å was set to avoid interactions with neighboring unit cells, and a $3 \times 3 \times 1$ Monkhorst-Pack *k*-point grid was used for optimization and energy calculations. The Van der Waals (vdW) effects were included using Grimme's DFT-D3 method [35,36]. The total energy and force convergence criteria were set to 10^{-5} eV and 0.02 eV/Å, respectively. The PHONOPY code was used to calculate phonon dispersion [37]. To obtain more accurate adsorption energies, zero-point energy corrections for H_2O, CO_2, C_2H_4, and C6-aldehyde interacting with pristine and doped C_3N were applied using VASPKIT [38]. Convergence tests for both the plane-wave cutoff energy and *k*-point density were performed to ensure total-energy convergence within 0.02 eV.

The binding energy (E_b) of C_3N with doping metal at C vacancy (V_C) and N vacancy (V_N) is defined as:

$$E_b = E_{\text{metal}-C_3N-V_{C/N}} - E_{C_3N-V_{C/N}} - E_{\text{metal}} \quad (1)$$

where E_{metal} is the total energy of isolated metal atoms, $E_{C_3N-V_{C/N}}$ and $E_{\text{metal}-C_3N-V_{C/N}}$ are the total energies of pristine C_3N with C and N vacancy, and C_3N with doped metal with C and N vacancy, respectively. A negative binding energy indicates that the metal atom is energetically favorable for binding to the defective C_3N monolayer.

The adsorption energy (E_{ads}) of a gas molecule on pristine C_3N, C_3N with vacancy ($V_{C/N}$), or metal-doped C_3N is calculated through the equation:

$$E_{ads} = E_{\text{system}-\text{gas}} - \left(E_{\text{system}} + E_{\text{gas}}\right), \quad (2)$$

where E_{system} and $E_{\text{system}\ -\ \text{gas}}$ are the total energies of pristine, C and N vacancies, and metal-doped C_3N before and after adsorbing the gas molecule, and E_{gas} is the energy of the isolated molecules. A negative adsorption energy indicates that the gas molecule is favorably adsorbed onto the C_3N monolayer.

To compute the charge difference, the following equation was used:

$$\Delta\rho = \rho_{\text{total}} - \rho_{\text{surface}} - \rho_{\text{gas}} \quad (3)$$

where ρ_{total} represents the total charge density of the adsorbed system, and ρ_{surface} and ρ_{gas} represent the charge densities of the isolated surface and the gas molecule, respectively. Using VESTA, we visualized the charge difference plots to pinpoint regions with charge accumulation (yellow) and charge depletion (cyan). This analysis offered insights into the electronic interactions and charge transfer between the gas molecules and the C_3N monolayer.

The work function was calculated for pristine C_3N, vacancies in C_3N ($V_{C/N}$), and metal-doped vacancies in C_3N before and after gas adsorption. The definition of work function (Φ) is the minimum energy needed to release electrons from the Fermi level (E_{Fermi}) to a vacuum (E_{vac}):

$$\Phi = E_{\text{vac}} - E_{\text{Fermi}} \quad (4)$$

The vacuum level (E_{vac}) was determined from the planar-averaged electrostatic potential in the vacuum region of the supercell. A dipole correction was applied along the direction perpendicular to the surface to remove artificial dipole interactions arising from the asymmetric slab geometry, ensuring reliable values. All work function calculations were performed after full structural relaxation. Since gas adsorption perturbs surface dipoles and charge distribution, the resulting work function variation provides a sensitive descriptor of adsorption-induced electronic effects and is widely used to evaluate gas-sensing performance [39].

The recovery time (τ) of the gas molecules desorbing from the C_3N surfaces was estimated using the following equation derived from transition-state theory:

$$\tau = \nu_0^{-1} \exp\left(\frac{-E_{ads}}{k_B T}\right) \quad (5)$$

where E_{ads} is the adsorption energy of the gas molecule on the surface, k_B is the Boltzmann constant, T is the temperature (300 K), and ν_0 is the attempt frequency. Here, we estimated it as the average optical phonon frequency of pristine C_3N, which is $\sim 4 \times 10^{13}$ s^{-1} for accurate recovery times. Recovery times were evaluated for H_2O, CO_2, C_2H_4, and C6-aldehyde on pristine and metal-doped C_3N monolayer. These results demonstrate the gas sensor's performance at room temperature. The shorter recovery times indicate faster desorption, while the longer recovery times show slower desorption of the gas molecule on the material's surface.

3. Results and discussion

3.1. Pristine C_3N monolayer: structure and electronic properties

The optimized primitive cell of monolayer C_3N exhibits a graphene-like planar structure with hexagonal symmetry. The calculated lattice constant is 4.861 Å, closely matching both previous theoretical reports and the experimental value of 4.75 Å [27]. The C–C and C–N bond lengths are 1.427 Å and 1.430 Å, respectively, further validating our computational approach. We identified six potential adsorption sites in the C_3N unit cell for gas adsorption studies. These sites are classified as top sites (above a carbon atom, T_C, or a nitrogen atom, T_N), bridge sites (above a C–C or C–N bond, B_{CC} and B_{CN}), and hollow sites (at the center of CC or CN rings, H_{CC} and H_{CN}), as illustrated in Fig. 1. Electronic band structure calculations indicate that pristine C_3N is an indirect bandgap semiconductor with a bandgap of 0.39 eV, with the valence band maximum (VBM) located at the M point and the conduction band minimum (CBM) at Γ. The projected density of states (PDOS) reveals dominant contributions from carbon and nitrogen p-orbitals near the Fermi level, indicating active sites for electronic modulation upon adsorption. Phonon dispersion calculations reveal no imaginary frequencies across the Brillouin zone, confirming the dynamic stability of the monolayer (see Fig. S1 in Supplementary Material). Additionally, the cohesive energy of –7.094 eV per atom affirms the thermodynamic robustness of the system. These results establish pristine C_3N as a stable 2D material with semiconducting properties suitable for sensing applications.

However, the relatively inert surface of pristine C_3N limits its interaction strength with gas molecules, which restricts its sensitivity and selectivity for practical sensing. To address this limitation, modification strategies such as vacancy creation and metal doping can be employed. These approaches are known to generate chemically active sites and alter local electronic structures, thereby enhancing gas adsorption and improving sensing performance. The following section, therefore, explores the stability and characteristics of vacancy formation and metal doping in C_3N.

3.2. Defect engineering and metal doping of C_3N monolayers

To enhance the gas adsorption capability of C_3N, point defects and metal doping strategies were explored, as it has been reported that Pd-doping on nitrogen vacancy enhances surface reactivity [40]. Specifically, we investigated single-atom vacancies by removing either a carbon atom (V_C) or a nitrogen atom (V_N) from the pristine lattice. Subsequent metal decoration was performed by introducing Na, Mg, or Al atoms into these vacancy sites. Binding energy calculations reveal that all metal dopants bind more favorably at V_C sites compared to V_N sites, indicating stronger thermodynamic stability. Among the dopants, Al exhibits the highest binding strength at the carbon vacancy site (–6.035 eV), followed by Mg (–3.188 eV) and Na (–2.089 eV). These results suggest that metal atoms are likely to be stabilized at vacancy sites rather than aggregating on the surface, thus preserving single-atom dispersion—a desirable feature for sensitive and selective gas detection. To further verify the thermodynamic stability of the doped structures, ab initio molecular dynamics (AIMD) simulations were performed at 300 K for 5 ps, confirming that the metal atoms remain firmly anchored at the V_C site without diffusion or detachment (see Fig. S2 in the Supplementary Material).

Charge density difference (CDD) analysis was performed to elucidate further the effect of metal doping on the local electronic environment (Fig. 2). Pronounced electron accumulation around the dopant atoms and depletion on adjacent C and N atoms were observed for Al-V_C and Mg-V_C, reflecting strong electronic coupling with the lattice. In contrast, Na-V_C showed weaker charge redistribution, indicating a less effective interaction. Bader charge analysis confirms this trend, with Al donating the largest charge to the lattice, followed by Mg and then Na. These electronic trends are consistent with geometric analysis: the nearest dopant–lattice bond lengths decrease in the order Na-V_C (2.37 Å) > Mg-V_C (2.02 Å) > Al-V_C (1.91 Å) (Table 1). The shorter Al–C/N and Mg–C/N bonds indicate stronger orbital overlap and enhanced stabilization, whereas the larger Na–C/N separation points to weaker binding. The combined charge redistribution and bond length analysis demonstrates that Al-V_C and Mg-V_C are the most effective doped configurations, providing electronically activated sites that favor stronger gas adsorption.

Structural optimization of the doped systems reveals mild to moderate out-of-plane distortions around the dopant sites, depending on atomic size and bonding strength. Such local changes further facilitate electronic activation of vacancy sites, thereby creating favorable conditions for gas–surface interactions. Based on these observations, the Na-V_C, Mg-V_C, and Al-V_C configurations were selected for detailed gas adsorption and sensing analysis in the following sections.

3.3. Structural properties of target gas molecules

Before performing adsorption calculations, the isolated structures of gas molecules, H_2O, CO_2, C_2H_4, and C6-aldehyde, were thoroughly optimized using DFT calculations. This step is essential for obtaining accurate reference energies and realistic molecular configurations for later interaction studies with C_3N-based surfaces. These gases were chosen for their importance as biomarkers of plant stress and their relevance to environmental sensing applications. The optimized H_2O structure showed a bent shape with an O–H bond length of 0.972 Å and an H–O–H bond angle of 104.5°, consistent with previous calculations

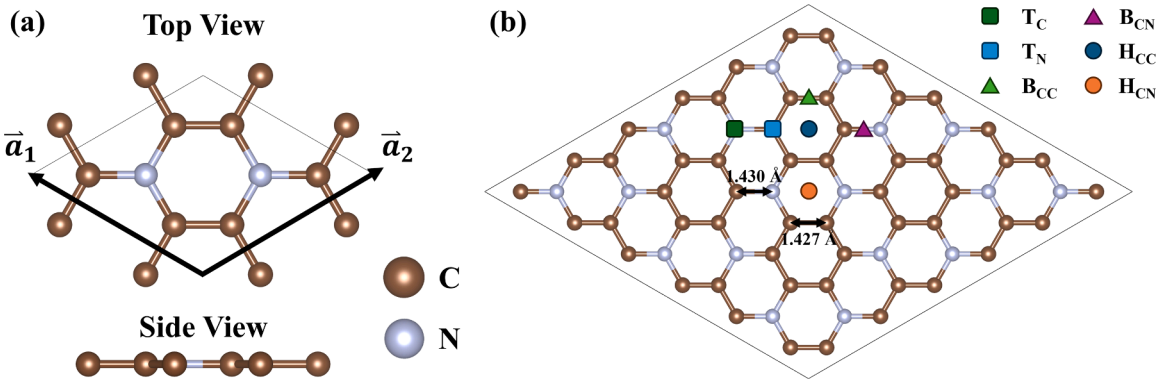

Fig. 1. (a) Top and side views of the primitive unit cell of monolayer C_3N, representing a two-dimensional carbon nitride structure. (b) Top view of the 3 × 3 × 1 supercell of C_3N, where six possible gas adsorption sites (T_C, T_N, B_{CC}, B_{CN}, H_{CC}, and H_{CN}) are shown. Brown and white spheres represent carbon and nitrogen atoms, respectively.

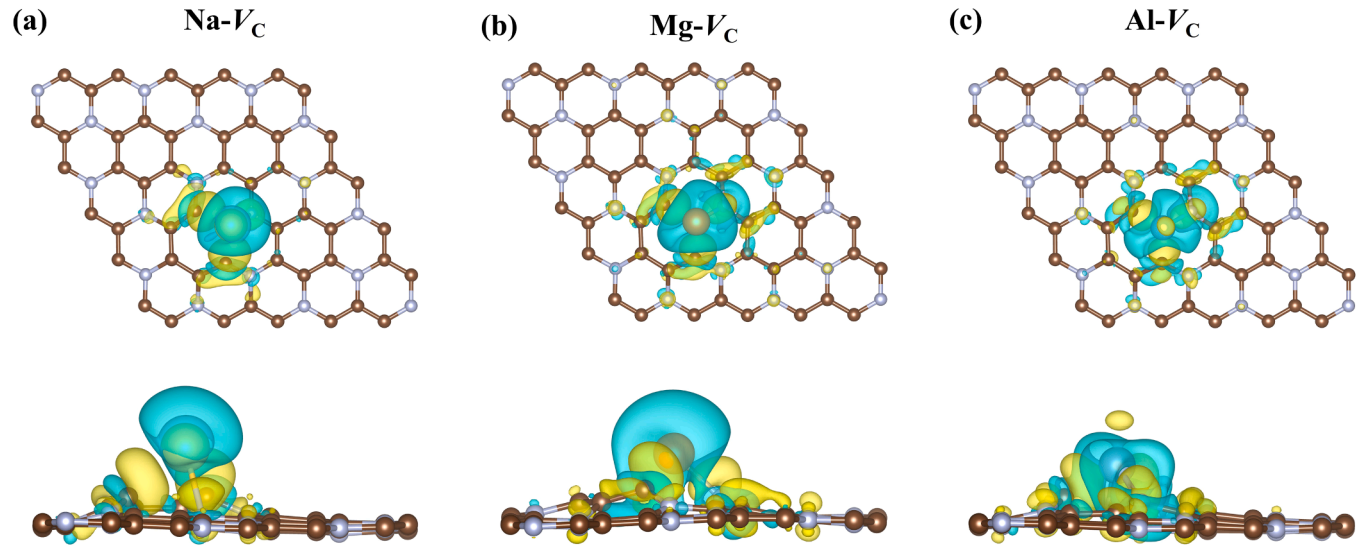

Fig. 2. Charge density difference plots of (a) Na-V_C, (b) Mg-V_C, and (c) Al-V_C C_3N systems. Yellow and cyan regions denote electron accumulation and depletion, respectively. The isosurfaces are visualized at 5 % of the maximum charge density difference for each system. Top and side views are shown for each system.

Table 1
Nearest distances (Å) between the dopant atom (Na, Mg, Al) and the adjacent C and N atoms in C_3N. The average distance is calculated from two nearest C atoms and one nearest N atom.

System	C (2 atoms) (Å)	N (1 atom) (Å)	Average distance (Å)
Na-V_C	2.343	2.425	2.370
Mg-V_C	2.034	1.989	2.019
Al-V_C	1.918	1.885	1.907

[41]. The CO_2 molecule was optimized to a linear form with C–O bond lengths of 1.177 Å, in excellent agreement with literature values [42]. Ethylene (C_2H_4), a planar molecule, had an optimized C=C double-bond length of 1.333 Å and C–H bond lengths of 1.091 Å, both of which matched previously reported theoretical values [10]. Our bond-length results for all molecules also agree well with experimental findings [43].

C6-aldehyde, a class of volatile organic compounds associated with plant stress signaling, exhibit greater conformational flexibility. To explore the adsorption of this molecule on the C_3N monolayer, ten candidate conformers were obtained from the PubChem database and optimized [44]. The five lowest-energy conformers were selected as representative ground-state structures and were consistently used as the initial adsorption configurations for all C_3N systems studied (pristine, Na-V_C, Mg-V_C, and Al-V_C). Each of these conformers was individually relaxed on each surface, and the configuration yielding the lowest adsorption energy was identified as the most stable adsorption state. This procedure ensures that the same conformer set and consistent selection criteria were applied to all systems, allowing reliable comparison of adsorption energies and subsequent electronic-structure analyses (see Table S1 in the Supplemental Material). After full structural relaxation of these gas–surface systems, the configuration yielding the strongest adsorption energy was retained for subsequent analyses, including electronic structure, work function, charge-transfer, and recovery-time calculations.

3.4. Adsorption characteristics of gas molecules on pristine and modified C_3N surfaces

The adsorption behaviors of H_2O, CO_2, C_2H_4, and C6-aldehyde molecules were systematically explored on pristine and modified C_3N surfaces, including vacancy-defective (V_C, V_N) and metal-doped (Na, Mg, Al at V_C) configurations. The calculated zero-point energy (ZPE)-corrected adsorption energies (E_{ads}) are summarized in Fig. 3. Pristine C_3N exhibited relatively weak adsorption strengths for all gases, with E_{ads} values between –0.1 eV and –0.6 eV, characteristic of physisorption and consistent with its chemically inert surface. Introduction of atomic vacancies moderately enhanced adsorption, particularly for C_2H_4 and H_2O at V_C, suggesting that the unsaturated sites created by atom removal provide localized centers that facilitate stronger gas–surface interactions. Metal doping at V_C sites markedly increased adsorption strength. Al-V_C exhibited strong interaction with CO_2 (≈ –1.0 eV), indicating robust chemisorption accompanied by substantial charge transfer. Mg-V_C exhibited the largest adsorption energies overall, with E_{ads} of –0.9 eV for H_2O and nearly –1.8 eV for C6-aldehyde, the latter reflecting the polarity and flexibility of the aldehyde molecule that enables close coupling with the Mg site. By contrast, Na-V_C showed weaker binding (typically –0.2 to –0.6 eV) but still stronger than pristine or vacancy-only surfaces.

To gain microscopic insight into these adsorption trends, optimized adsorption geometries and CDD plots were analyzed. Representative results for Mg-V_C are shown in Fig. 4, while the corresponding Na-V_C and Al-V_C cases are provided in the Supplementary Material (Figs. S3–S4). For Mg-V_C, adsorbed gases are stabilized at distances of 2.07–2.47 Å from the surface, with pronounced electron accumulation and depletion

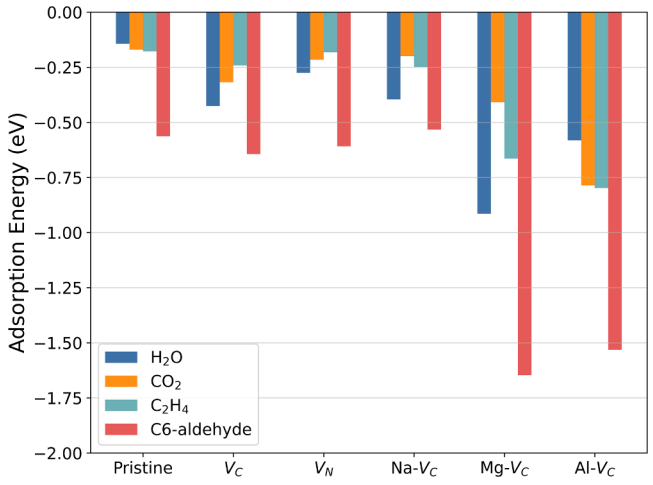

Fig. 3. Adsorption energies of H_2O, CO_2, C_2H_4, and C6-aldehyde molecules on pristine and modified C_3N surfaces.

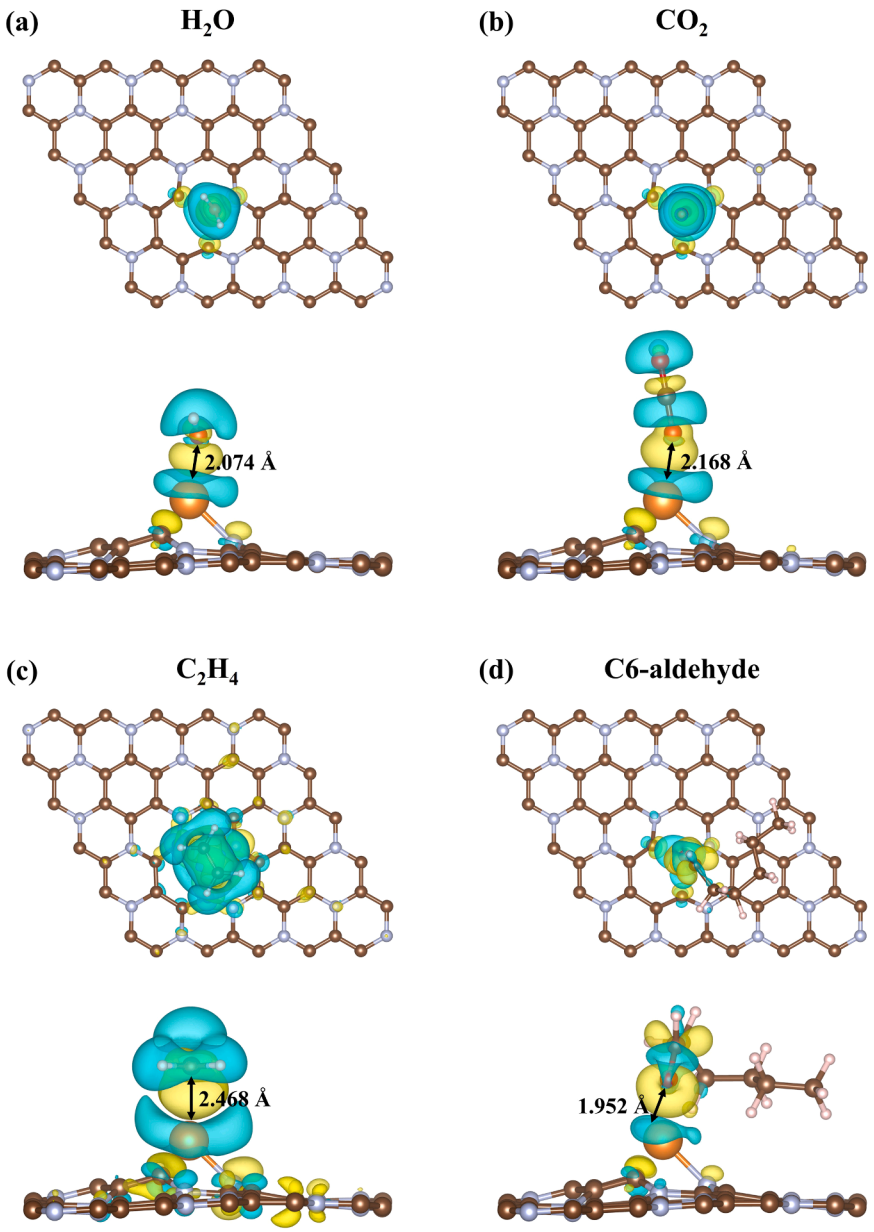

Fig. 4. Optimized adsorption geometries and charge density difference plots of (a) H_2O, (b) CO_2, (c) C_2H_4, and (d) C6-aldehyde molecules on Mg-doped C_3N (Mg-V_C). Interfacial distances between the adsorbate and the doped surface are indicated. The isosurface level of the charge distribution was set to 5 % of the maximum.

features observed particularly for CO_2 and C6-aldehyde. These redistribution patterns confirm strong orbital overlap and significant charge transfer, consistent with the large adsorption energies discussed above.

Comparison with the other dopants reveals a clear hierarchy. Al-V_C also shows notable charge redistribution, especially for CO_2 adsorption, in line with its strong E_{ads} value, though its interactions with H_2O and C_2H_4 are less pronounced. In contrast, Na-V_C exhibits weaker electron redistribution and larger equilibrium distances (>2.3 Å), consistent with its relatively modest adsorption energies. Taken together, these results show that Mg- and Al-doped C_3N generate highly active adsorption sites that can strongly interact with polar or reactive gas molecules, whereas Na doping offers only moderate improvements.

3.5. Electronic response to gas adsorption: work function and charge transfer

The electronic response of C_3N-based systems upon gas adsorption was examined by measuring changes in work function (Φ) and performing Bader charge-transfer analysis. The work function reflects the minimum energy required to remove an electron from the Fermi level to the vacuum level, and adsorption-induced shifts in Φ serve as a sensitive indicator of surface dipole changes and electronic redistribution. Such changes are directly relevant to field-effect transistors and Kelvin probe-based sensors, where gas detection depends on measurable changes in the work function (ΔΦ) upon adsorption. FET-type transducers have been shown to convert these ΔΦ into threshold voltage shifts [45,46], and work-function probes such as Kelvin-probe force microscopy measure contact potential differences consistent with gas adsorption events [47,48].

Fig. 5 summarizes the calculated work functions for pristine, vacancy-defective (V_C, V_N), and metal-doped (Na-, Mg-, and Al-V_C) C_3N surfaces before and after adsorption of H_2O, CO_2, C_2H_4, and C6-aldehyde. Adsorption generally increased ΔΦ relative to the gas-free state, consistent with electron transfer from the substrate to the adsorbed molecule. The most pronounced effect occurred for CO_2 adsorption on Al-V_C, where the work function increased from ~3.4 eV (no gas) to

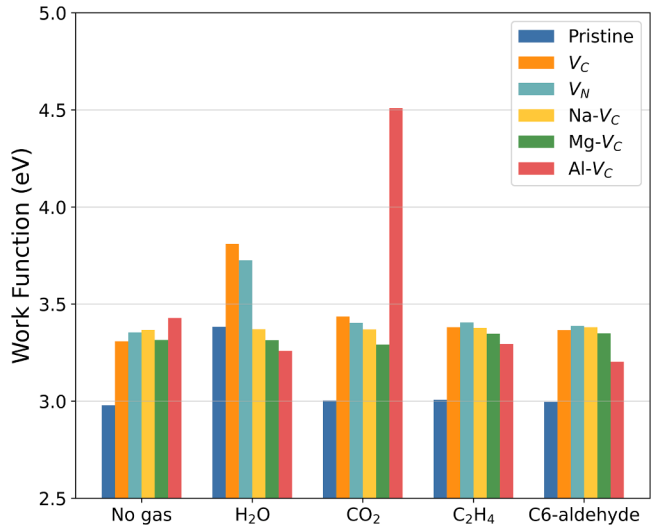

Fig. 5. Work function variations of pristine, vacancy-defective (V_C, V_N), and metal-doped (Na-, Mg-, Al-V_C) C_3N surfaces before and after adsorption of H_2O, CO_2, C_2H_4, and C6-aldehyde molecules.

~4.5 eV. This substantial shift indicates a strong electronic perturbation and correlates with the high adsorption energy and charge transfer observed for this configuration, underscoring the potential of Al-doped C_3N for highly sensitive CO_2 detection. Mg-V_C also showed notable increases in work function, particularly for H_2O and CO_2, consistent with the enhanced adsorption discussed in Section 3.4. By contrast, Na-V_C and pristine C_3N showed comparatively small shifts (<0.3 eV), consistent with their weaker adsorption strengths and limited charge redistribution.

To further clarify the origin of the observed work function changes, we analyzed the charge redistribution upon gas adsorption using Bader charge analysis. Table 2 summarizes the net charge transfer (Q_{tot}) between the surface and the adsorbed gas molecules for pristine, vacancy-defective, and metal-doped C_3N. Negative values correspond to electron transfer from the substrate to the adsorbate, while positive values indicate back-donation.

Bader charge analyses (Tables S3–S6) further clarify the microscopic origin of the observed changes in work function. For H_2O adsorption (Table S3), the charge transfer was generally small, reflecting a weak interaction. The largest electron donation from the substrate to the molecule was observed for Al-V_C (–0.100*e*) and Mg-V_C (–0.055*e*), consistent with their moderate work function increases. Interestingly, Na-V_C exhibited a slight back-donation (+0.029*e*), suggesting weaker coupling and corroborating its minimal electronic response. For CO_2 (Table S4), charge redistribution was much stronger. Al-V_C exhibited the most significant charge transfer (–1.055*e*), accompanied by a substantial work function increase (~1.1 eV), indicating a strong chemisorptive interaction. In contrast, pristine, V_C, V_N, and Mg-V_C transferred only ~–0.03*e* to –0.05*e*, while Na-V_C even displayed negligible net transfer (+0.013*e*). These results confirm Al doping as the most effective strategy for enhancing CO_2 sensitivity. Adsorption of C_2H_4 (Table S5) produced smaller charge transfers across all systems, consistent with its weaker adsorption energies. Nevertheless, Al-V_C (–0.332*e*) and Mg-V_C (–0.077*e*) induced measurable redistribution, while pristine, V_C, and V_N showed only modest values (≈ –0.070*e*). Na-V_C again exhibited charge back-donation (+0.028*e*), reinforcing its limited effectiveness for C_2H_4 detection.

C6-aldehyde molecules (Table S6) exhibited the most substantial charge transfer after CO_2. Al-V_C (–0.667*e*) and Mg-V_C (–0.445*e*) were dominant, confirming strong orbital hybridization with the dopant site and explaining their large adsorption energies and pronounced work function shifts. In comparison, pristine, V_C, and V_N transferred –0.137*e* to –0.188*e*, while Na-V_C contributed only –0.029*e*, consistent with weak sensitivity.

Taken together, the Bader charge results indicate two distinct sensing behaviors. Al-V_C stands out for CO_2, where the large electron transfer explains both its high adsorption energy and the strong work-function shift. Mg-V_C, on the other hand, interacts more strongly with polar molecules such as H_2O and C6-aldehyde, which is consistent with its moderate to large charge-transfer values for these gases. In contrast, Na-V_C shows little or even reversed charge redistribution, which helps to explain its weaker sensing response across all cases. These comparisons show that the type of dopant not only alters the strength of adsorption but also fine-tunes the selectivity of C_3N toward different classes of gas molecules.

To further elucidate the microscopic origin of the work function and charge transfer trends, we analyzed the projected density of states (PDOS) for selected gas–C_3N systems (Fig. 6). These spectra provide direct evidence of orbital hybridization between adsorbed molecules and substrate states, thereby clarifying how adsorption modifies the electronic structure.

The PDOS spectra clarify how adsorption perturbs the electronic structure. For H_2O on pristine C_3N (Fig. 6(a)), states near the Fermi level are essentially unaffected, and the molecular contributions remain well below E_F. This indicates minimal hybridization and is consistent with weak physisorption, small charge transfer, and minimal work-function change. In contrast, strong-interaction cases exhibit clear hybridization features: for CO_2 on Al-V_C (Fig. 6(b)), additional spectral weight appears near E_F, accompanied by broadening of the CO_2-derived states, reflecting strong coupling with Al-3*p* orbitals. This behavior correlates directly with the significant electron uptake (–1.055*e*), substantial adsorption energy (≈ –1.0 eV), and the pronounced increase in work function, confirming chemisorption. For C6-aldehyde on Mg-V_C (Fig. 6 (c)), overlap between molecular and Mg-related states a few eV below E_F indicates appreciable hybridization, consistent with the sizable charge transfer (–0.445*e*) and slow desorption kinetics. By comparison, Na-V_C shows only modest PDOS changes near E_F across all gases, matching its weaker adsorption and limited charge redistribution. These observations demonstrate that the degree of orbital hybridization in PDOS directly governs the measured charge transfer, adsorption strength, and work-function shifts. The complete set for all gas-surface combinations is provided in the Supplementary Material (Figs. S5–S10).

The strong correlation among adsorption energy, charge transfer, and work-function modulation demonstrates that structural modifications of C_3N directly influence its sensing response. These results demonstrate that adsorption energy, charge transfer, and work-function shifts are closely connected, and together they describe the thermodynamic and electronic response of C_3N surfaces to gas exposure. However, adsorption strength alone does not determine sensing performance. For a practical sensor, the material must also release adsorbed molecules efficiently, allowing the device to return to its baseline state and be reused. This motivates an examination of desorption kinetics, discussed next in Section 3.6.

Table 2
Net charge transfer (Q_{tot}, in *e*) from C_3N surfaces to adsorbed gas molecules, obtained from Bader charge analysis. Negative values indicate electron transfer from substrate to adsorbate.

System	H_2O	CO_2	C_2H_4	C6-aldehyde
Pristine	–0.027	–0.032	–0.072	–0.137
V_C	–0.036	–0.045	–0.072	–0.188
V_N	–0.047	–0.043	–0.073	–0.173
Na-V_C	+0.029	+0.013	+0.028	–0.029
Mg-V_C	–0.055	–0.046	–0.077	–0.445
Al-V_C	–0.100	–1.055	–0.332	–0.667

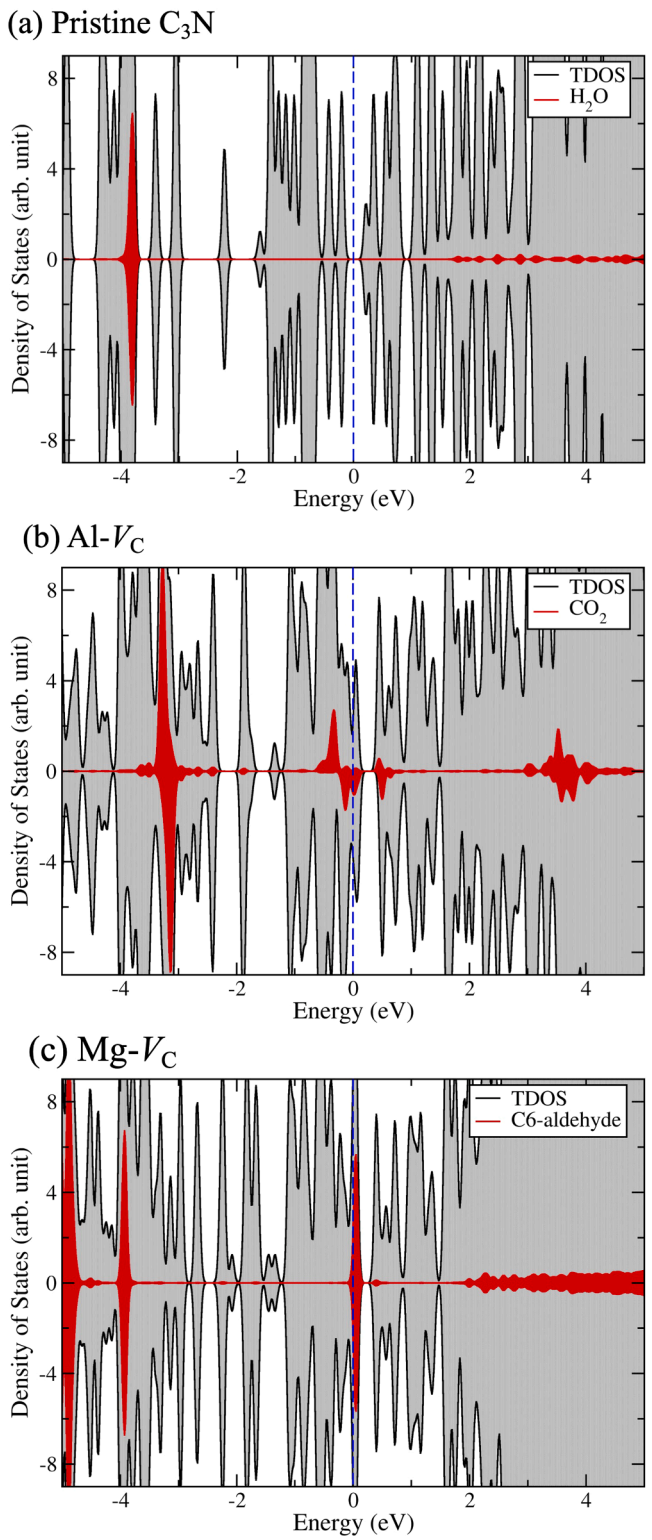

Fig. 6. Projected density of states (PDOS) for representative gas–C_3N systems: (a) H_2O on pristine C_3N, (b) CO_2 on Al-V_C, and (c) C6-aldehyde on Mg-V_C. The Fermi level (E_F) is set to 0 eV (dashed line).

3.6. Recovery time and desorption characteristics

Beyond the thermodynamic descriptors discussed earlier, the ability of a sensing material to restore its clean state is equally crucial. Recovery time (τ) reflects how quickly an adsorbed molecule desorbs from the surface and therefore determines response speed, reusability, and long-term stability. To quantify this aspect, recovery times (τ) were estimated using transition state theory, as shown in Fig. 7.

Pristine C_3N exhibits extremely short recovery times across all four gases, ranging from 10^{-11} to 10^{-12} s. Such rapid desorption confirms weak physisorption and facile reversibility, making pristine C_3N suitable for fast-response detection; however, this also limits its sensitivity due to the low adsorption strength. Introducing vacancies moderately increases recovery times. For instance, V_C shows longer desorption times for H_2O (3.5×10^{-7} s) and C6-aldehyde (1.6×10^{-3} s), while V_N exhibits similar behavior. These results indicate that vacancy-induced sites strengthen gas binding while maintaining reversibility.

Metal doping produces a broader range of recovery behaviors. Al-V_C displays significantly slower desorption for C6-aldehyde (1.4×10^{12} s), suggesting nearly irreversible adsorption under ambient conditions, though recovery times for smaller molecules remain within practical limits. Mg-V_C shows the longest recovery time overall, reaching ~10^{14} s for C6-aldehyde, reflecting its very strong adsorption affinity. Even for H_2O, Mg-V_C requires ~58 s for desorption, indicating sluggish recovery. By contrast, Na-V_C exhibits intermediate recovery times across all gases—for example, 2.2×10^{-5} s for C6-aldehyde—representing a compromise between sensitivity and reusability.

These results reveal a clear trade-off: stronger adsorption enhances sensitivity but hinders recovery, while weaker adsorption supports fast sensor reset but limits detection strength. Al- and Mg-doped systems offer high selectivity for CO_2 and C6-aldehyde, respectively, but at the cost of slow recovery, whereas Na-V_C provides a balanced sensing profile. This sensitivity–recovery trade-off is a key design consideration for tailoring C_3N-based sensors toward specific agricultural applications.

To provide a concise overview of the sensing performance, Table 3 summarizes the key parameters for all systems, including adsorption energy (E_{ads}), work-function shift (ΔΦ), and recovery time (τ) for each target gas. The optimal dopant ("best performer") for each gas is identified based on the balance between adsorption strength, sensitivity, and desorption kinetics. Al-V_C exhibits superior response to CO_2 owing to its strong chemisorption and large ΔΦ, while Mg-V_C is most effective for polar molecules such as H_2O and C6-aldehyde. Na-V_C provides moderate

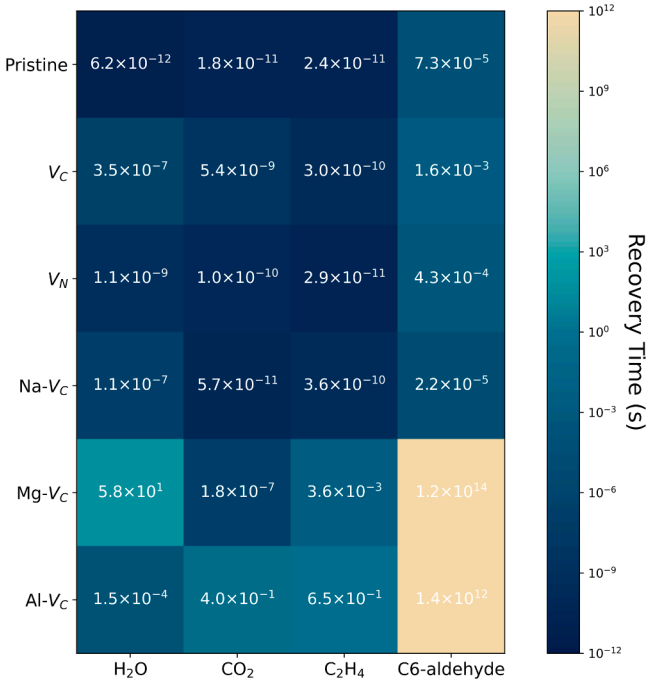

Fig. 7. Recovery times for desorption of H_2O, CO_2, C_2H_4, and C6-aldehyde molecules on pristine, vacancy-defective (V_C, V_N), and metal-doped (Na-, Mg-, Al-V_C) C_3N surfaces.

Table 3
Summarizes the key parameters for all systems, including adsorption energy (E_{ads}), work-function shift ($\Delta\Phi$), and recovery time (τ) for each target gas.

Gas molecule	Best dopant	E_{ads}(eV)	$\Delta\Phi$ (eV)	τ (s)
H_2O	Mg-V_C	–0.915	–0.001	5.8×10^{1}
CO_2	Al-V_C	–0.786	+1.081	4.0×10^{-1}
C_2H_4	Al-V_C	–0.798	–0.134	6.5×10^{-1}
C6-aldehyde	Mg-V_C	–1.647	+0.034	1.2×10^{14}

adsorption and fast recovery, making it suitable for reusable sensors.

3.7. Sensitivity and selective detection capability

Sensitivity (S) in gas sensors is defined as the relative change in an observable electronic parameter upon gas adsorption. In work-function-based sensors, the adsorption of gas molecules redistributes the surface charge, thereby altering the work function (Φ). This change can be directly related to sensor response using:

$$S(\%) = \frac{|\Phi_{ads} - \Phi_{clean}|}{\Phi_{clean}} \times 100\ \%, \quad (6)$$

where Φ_{ads} and Φ_{clean} are the work functions of the surface with and without adsorbed gas molecules, respectively. Changes in Φ reflect shifts in surface dipole and band bending, both well-established mechanisms in work-function-type sensors. For instance, studies on metal oxides and 2D materials confirm that gas adsorption induces detectable changes in Φ, thereby serving as a reliable sensing signal [39,49,50]. While other sensing metrics, such as band-gap modulation or conductivity changes, may also be used to estimate sensitivity, extracting reliable band-edge positions after doping or adsorption is often challenging because partial orbital occupation can lead to Fermi-level pinning. For this reason, work-function modulation provides a more robust and experimentally accessible indicator of sensitivity. In addition, changes in Φ are directly related to conductivity-based sensing mechanisms through adsorption-induced variations in carrier density and band alignment.

Fig. 8 presents the calculated sensitivities for H_2O, CO_2, C_2H_4, and C6-aldehyde on pristine, vacancy-defective, and metal-doped C_3N surfaces. Pristine C_3N shows very low sensitivity (<2 %) for all gases, reflecting weak adsorption and minimal electronic perturbation.

Vacancy creation slightly improves performance, with values reaching ~5–7 % for H_2O and CO_2 at V_C. Metal doping produces much stronger responses. Al-V_C exhibits exceptional sensitivity to CO_2, exceeding 30 %, which aligns with its high adsorption energy (≈ –1.0 eV) and strong charge transfer (–1.055*e*). Mg-V_C exhibits pronounced sensitivity to C6-aldehyde (~8 %) and a noticeable response to H_2O, consistent with its strong binding affinity and charge redistribution. Na-V_C demonstrates moderate sensitivity (~2–5 %) across all gases, suggesting a more balanced sensing capability without strong selectivity.

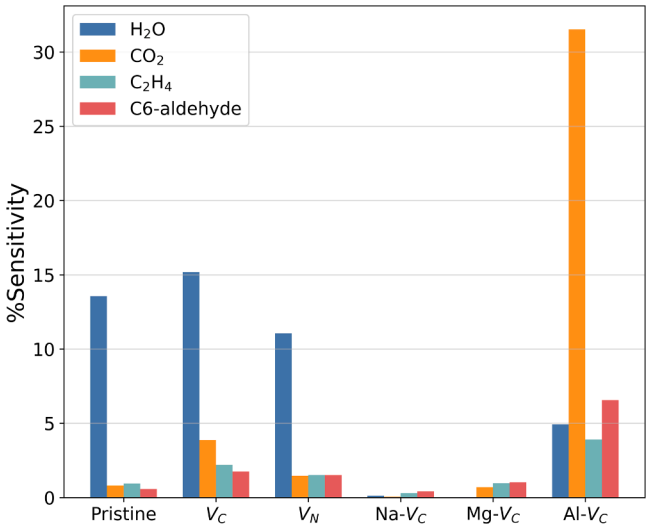

Fig. 8. Sensitivity (%) based on work function changes for H_2O, CO_2, C_2H_4, and C6-aldehyde adsorption on pristine and modified C_3N.

These results highlight a tunable selectivity hierarchy: Al-V_C is highly suited for CO_2 detection, Mg-V_C favors larger polar molecules such as C6-aldehyde, and Na-V_C provides a compromise between sensitivity and reusability. The strong correlation between adsorption energy, charge transfer, and sensitivity underscores the role of vacancy and dopant engineering in tailoring C_3N-based monolayers for application-specific gas-sensing tasks.

3.8. Practical implications and sensor design considerations

The findings presented in this study have significant implications for the practical development of sensors, particularly in agricultural and environmental monitoring applications. The demonstrated capability to tailor adsorption strength, electronic response, and recovery behavior through vacancy engineering and metal doping of C_3N monolayers provides clear avenues for optimizing sensor performance.

For applications that demand rapid response and frequent reuse, such as continuous, real-time monitoring, materials exhibiting moderate adsorption strengths and balanced recovery times, like Na-V_C, are highly suitable. Conversely, in scenarios where sensitivity and selectivity are paramount, such as detecting trace-level plant stress indicators or specific environmental pollutants, Al- and Mg-doped surfaces offer distinct advantages despite their longer recovery times. Target gas characteristics should guide the selection of particular surface modifications (vacancies or dopants), as well as the desired sensitivity levels, acceptable recovery periods, and optimal operational conditions. Additionally, incorporating metal-doped C_3N into practical sensor devices such as field-effect transistors (FETs) or chemiresistors requires careful consideration of reproducibility, stability under realistic environmental conditions, and compatibility with existing fabrication processes.

Plant-emitted gases during stress typically occur within the ppb–ppm range. For example, CO_2 concentrations around stomatal pores can fluctuate by several hundred ppm, ethylene (C_2H_4) commonly rises to ~0.1–1 ppm, and C6-aldehydes can reach ~10 ppm near damaged or drought-affected tissues, while drought conditions also lead to a noticeable reduction in local H_2O vapor due to suppressed transpiration [3]. These experimentally observed concentration ranges are consistent with our calculated adsorption trends: weak-to-moderate adsorption on pristine C_3N (−0.1 to −0.6 eV) is suitable for detecting large fluctuations in CO_2 and H_2O vapor, whereas the strong adsorption energies obtained for Al-V_C and Mg-V_C (up to −1.0 to −1.8 eV) align well with the sensitivity required for low-ppm detection of stress-related VOCs. This correspondence between realistic concentration levels and adsorption energetics reinforces the practical suitability of doped C_3N monolayers for agricultural gas-sensing applications.

4. Conclusion

In summary, our results show that introducing vacancies together with metal dopants significantly improves the gas-sensing performance of C_3N relative to pristine and previously studied C_3N systems. Al substitution at V_C produces a strong CO_2 adsorption energy of about –1.0 eV and the largest charge transfer (–1.055*e*), giving rise to a substantial work-function shift of roughly 1.1 eV. This response is much larger than the small shifts (<0.3 eV) typically reported for undoped C_3N. Mg-V_C interacts most strongly with C6-aldehydes, reaching adsorption energies up to –1.8 eV with sizable charge transfer (–0.445*e*), which is far above values previously calculated for small, nonpolar analytes. These electronic changes translate into notable sensing responses, including >30 % sensitivity for CO_2 on Al-V_C and around 8 % for C6-aldehyde on Mg-

V_C.

The improved interactions are accompanied by distinct kinetic behaviors: Al- and Mg-doped systems desorb more slowly, whereas Na-V_C maintains moderate adsorption energies and rapid recovery, making it a more reusable sensing platform. These dopant-dependent trends establish clear design rules for tuning C_3N selectivity and guide its use for detecting agriculturally relevant gases. These computational results provide practical guidelines for experimental validation and device development. The dopant-dependent enhancements in adsorption strength and electronic response identified here can directly inform future fabrication and testing of C_3N-based FET or chemiresistive gas sensors for agricultural applications.

Declaration of generative AI and AI-assisted technologies in the manuscript preparation process

During the preparation of this manuscript, the authors used ChatGPT (OpenAI) and Grammarly to refine the English language and improve clarity. After using these tools, the authors reviewed and edited the content and take full responsibility for the published article.

CRediT authorship contribution statement

Watcharin Teeranattapong: Writing – review & editing, Writing – original draft, Visualization, Investigation, Formal analysis, Data curation. **Audomsak Sripothongnack:** Writing – review & editing, Investigation. **Thanasee Thanasarnsurapong:** Writing – review & editing, Methodology. **Chatchawal Wongchoosuk:** Writing – review & editing, Conceptualization. **Pakpoom Reunchan:** Writing – review & editing, Writing – original draft, Supervision, Investigation, Funding acquisition, Conceptualization.

Declaration of competing interest

The authors declare that they have no known competing financial interests or personal relationships that could have appeared to influence the work reported in this paper.

Acknowledgements

This work was supported by the Kasetsart Research and Development Institute (KURDI) under Grant No FF(KU)55.69. W.T. acknowledges the Graduate Fellowship Program from the Faculty of Science, Kasetsart University. We thank the NSTDA Supercomputer Center (ThaiSC) for providing the computing resources used in this work.

Supplementary materials

Supplementary material associated with this article can be found, in the online version, at doi:10.1016/j.surfin.2025.108318.

Data availability

Data will be made available on request.

References

[1] M.E. Bergman, X.-Q. Huang, S. Baudino, J.-C. Caissard, N. Dudareva, Plant volatile organic compounds: emission and perception in a changing world, Curr. Opin. Plant Biol. 85 (2025) 102706.
[2] S. Jamalzadegan, J. Xu, Y. Shen, B. Mativenga, M. Li, M. Zare, A. Penumudy, Z. Hetzler, Y. Zhu, Q. Wei, Advancing wearable VOC sensors: a roadmap for sustainable agriculture and real-time plant health monitoring, Chem. Bio. Eng. 2 (2025) 460–474.
[3] P. Coatsworth, L. Gonzalez-Macia, A.S.P. Collins, T. Bozkurt, F. Güder, Continuous monitoring of chemical signals in plants under stress, Nat. Rev. Chem. 7 (2023) 7–25.
[4] N. Tuteja, S.K. Sopory, Chemical signaling under abiotic stress environment in plants, Plant Signal Behav. 3 (2008) 525–536.
[5] T. Seesaard, K. Kamjornkittikoon, C. Wongchoosuk, A comprehensive review on advancements in sensors for air pollution applications, Sci. Total Environ. 951 (2024) 175696.
[6] T. Seesaard, N. Goel, M. Kumar, C. Wongchoosuk, Advances in gas sensors and electronic nose technologies for agricultural cycle applications, Comput. Electron. Agric. 193 (2022) 106673.
[7] S. Yang, C. Jiang, S.-H. Wei, Gas sensing in 2D materials, Appl. Phys. Rev. 4 (2017) 021304.
[8] E. Llobet, Gas sensors using carbon nanomaterials: a review, Sens. Actuators B: Chem. 179 (2013) 32–45.
[9] F. Schedin, A.K. Geim, S.V. Morozov, E.W. Hill, P. Blake, M.I. Katsnelson, K. S. Novoselov, Detection of individual gas molecules adsorbed on graphene, Nat. Mater. 6 (2007) 652–655.
[10] A.S. Rad, Adsorption of C_2H_2 and C_2H_4 on Pt-decorated graphene nanostructure: ab-initio study, Synth. Met. 211 (2016) 115–120.
[11] M. Kaur, M. Kaur, V.K. Sharma, Nitrogen-doped graphene and graphene quantum dots: a review onsynthesis and applications in energy, sensors and environment, Adv. Colloid Interface Sci. 259 (2018) 44–64.
[12] T. Movlarooy, A. Nooranbjar, Gas molecules adsorption on the α-Graphyne nanosheet for the sensor applications, Diam. Relat Mater. 148 (2024) 111471.
[13] S. Kim, P. Gamallo, F. Viñes, J.Y. Lee, The nano gold rush: graphynes as atomic sieves for coinage and Pt-group transition metals, Appl. Surf Sci. 499 (2020) 143927.
[14] P. Li, J. Yu, C. Cao, W. Song, Graphdiyne: a highly sensitive material for ppb-level NO_2 gas sensing at room temperature, Chem. Res. Chin. Univ. 37 (2021) 1317–1322.
[15] D.-F. Ma, H.-Q. Liu, X.-Y. Zhang, Y.-N. Jia, X. Zhang, F. Niu, K.-F. Zhang, Y.-Q. Zhao, N-doped graphdiyne derivative for highly selective and ultrasensitive NH3 sensing at room temperature, Phys. Chem. Chem. Phys. 27 (2025) 5732–5738.
[16] L. Zhang, B. He, Y. Li, J. Yun, L. Yao, H. Zhao, J. Yan, W. Zhao, Z. Zhang, Nitrogen-doped graphyne as a promising material for sensing volatile organic compounds in Human breath, ACS Sens. 10 (2025) 2499–2509.
[17] R. Lv, Q. Li, A.R. Botello-Méndez, T. Hayashi, B. Wang, A. Berkdemir, Q. Hao, A. L. Elías, R. Cruz-Silva, H.R. Gutiérrez, Y.A. Kim, H. Muramatsu, J. Zhu, M. Endo, H. Terrones, J.-C. Charlier, M. Pan, M. Terrones, Nitrogen-doped graphene: beyond single substitution and enhanced molecular sensing, Sci. Rep. 2 (2012) 586.
[18] T. Thanasarnsurapong, S. Sringamprom, P. Reunchan, W. Sirisaksoontorn, S. Jungthawan, P. Nedkun, J. Prasongkit, A. Boonchun, Strong toxic gas detection on penta-BCP monolayers: insights from DFT calculations, Talanta Open 11 (2025) 100412.
[19] R. Rahimi, M. Solimannejad, A. Horri, DFT study of the adsorption properties and sensitivity of a B2N monolayer toward harmful gases, Sci. Rep. 14 (2024) 29282.
[20] C. Wang, Y. Wang, Z. Yang, N. Hu, Review of recent progress on graphene-based composite gas sensors, Ceram Int. 47 (2021) 16367–16384.
[21] Y. Yong, H. Cui, Q. Zhou, X. Su, Y. Kuang, X. Li, C_2N monolayer as NH3 and NO sensors: a DFT study, Appl. Surf. Sci. 487 (2019) 488–495.
[22] X. Shi, W. An, Y. Li, Y. Wang, E. Dai, M. Liu, R. Guo, J. Wang, Heteroatom decorated C2N monolayer for gas-sensing application: insight from first-principles, J. Chem. Phys. 162 (2025).
[23] P. Chalase, S. Deshpande, S. Kumavat, M. Deshpande, Adsorption mechanism of different toxic gases onto pristine BNC2 and Al-doped BNC2 monolayers, Phys. Chem. Chem. Phys. 25 (2023) 17337–17351.
[24] A. Sripothongnack, W. Teeranattapong, A. Ananchuensook, T. Thanasarnsurapong, J. T-Thienprasert, C. Wongchoosuk, P. Reunchan, Unveiling the role of metal-doped BNC_2 monolayer for selective gas adsorption: a DFT investigation, Surf. Interfaces 56 (2025) 105481.
[25] S. Yang, W. Li, C. Ye, G. Wang, H. Tian, C. Zhu, P. He, G. Ding, X. Xie, Y. Liu, Y. Lifshitz, S.-T. Lee, Z. Kang, M. Jiang, C_3N—A 2D crystalline, hole-free, tunable-narrow-bandgap semiconductor with ferromagnetic properties, Adv. Mater. 29 (2017) 1605625.
[26] Z. Chen, H. Wang, Z. Li, First-principles study of two dimensional C3N and its derivatives, RSC Adv. 10 (2020) 33469–33474.
[27] J. Mahmood, E.K. Lee, M. Jung, D. Shin, H.-J. Choi, J.-M. Seo, S.-M. Jung, D. Kim, F. Li, M.S. Lah, N. Park, H.-J. Shin, J.H. Oh, J.-B. Baek, Two-dimensional polyaniline (C_3N) from carbonized organic single crystals in solid state, Proc. Natl. Acad. Sci. 113 (2016) 7414–7419.
[28] V. Babar, S. Sharma, U. Schwingenschlögl, Highly sensitive sensing of NO and NO_2 gases by Monolayer C_3N, Adv. Theory Simul. 1 (2018) 1700008.
[29] M. Pashangpour, A.A. Peyghan, Adsorption of carbon monoxide on the pristine, B- and Al-doped C_3N nanosheets, J. Mol. Model 21 (2015) 116.
[30] G. Kresse, J. Hafner, Ab initio molecular dynamics for liquid metals, Phys. Rev. B 47 (1993) 558–561.
[31] G. Kresse, J. Furthmüller, Efficiency of ab-initio total energy calculations for metals and semiconductors using a plane-wave basis set, Comput. Mater. Sci. 6 (1996) 15–50.
[32] P.E. Blöchl, Projector augmented-wave method, Phys. Rev. B 50 (1994) 17953–17979.
[33] J.P. Perdew, K. Burke, M. Ernzerhof, Generalized gradient approximation made simple, Phys. Rev. Lett 77 (1996) 3865–3868.
[34] H.J. Monkhorst, J.D. Pack, Special points for Brillouin-zone integrations, Phys. Rev. B 13 (1976) 5188–5192.
[35] S. Grimme, S. Ehrlich, L. Goerigk, Effect of the damping function in dispersion corrected density functional theory, J. Comput. Chem. 32 (2011) 1456–1465.

[36] S. Grimme, J. Antony, S. Ehrlich, H. Krieg, A consistent and accurate ab initio parametrization of density functional dispersion correction (DFT-D) for the 94 elements H-Pu, J. Chem. Phys. 132 (2010) 154104.
[37] A. Togo, I. Tanaka, First principles phonon calculations in materials science, Scr. Mater. 108 (2015) 1–5.
[38] V. Wang, N. Xu, J.-C. Liu, G. Tang, W.-T. Geng, VASPKIT: a user-friendly interface facilitating high-throughput computing and analysis using VASP code, Comput. Phys. Commun. 267 (2021) 108033.
[39] A. Oprea, N. Bârsan, U. Weimar, Work function changes in gas sensitive materials: fundamentals and applications, Sens. Actuators B: Chem. 142 (2009) 470–493.
[40] H. Cui, Z. Liu, P. Jia, Pd-doped C_3N monolayer: a promising low-temperature and high-activity single-atom catalyst for CO oxidation, Appl. Surf. Sci. 537 (2021) 147881.
[41] Y. Chen, Y. Gui, X. Chen, Adsorption and gas-sensing properties of C_2H_4, CH_4, H_2, H_2O on metal oxides (CuO, NiO) modified SnS_2 monolayer: a DFT study, Results Phys. 28 (2021) 104680.
[42] X. Li, T. Guo, L. Zhu, C. Ling, Q. Xue, W. Xing, Charge-modulated CO_2 capture of C_3N nanosheet: insights from DFT calculations, Chem. Eng. J. 338 (2018) 92–98.
[43] National Institute of Standards and Technology (NIST), Computational Chemistry Comparison and Benchmark Database (CCCBDB) (accessed September 9, 2025). https://cccbdb.nist.gov/expdatax.asp.
[44] National Center for Biotechnology Information (NCBI), PubChem Compound Summary for CID 6184: Hexanal, PubChem Database, U.S, National Library of Medicine (accessed July 7, 2025) https://pubchem.ncbi.nlm.nih.gov/compound/Hexanal.
[45] P. Bergveld, J. Hendrikse, W. Olthuis, Theory and application of the material work function for chemical sensors based on the field effect principle, Meas. Sci. Technol. 9 (1998) 1801.
[46] M. Burgmair, H.P. Frerichs, M. Zimmer, M. Lehmann, I. Eisele, Field effect transducers for work function gas measurements: device improvements and comparison of performance, Sens. Actuators B: Chem. 95 (2003) 183–188.
[47] D. Ziegler, P. Gava, J. Güttinger, F. Molitor, L. Wirtz, M. Lazzeri, A.M. Saitta, A. Stemmer, F. Mauri, C. Stampfer, Variations in the work function of doped single- and few-layer graphene assessed by Kelvin probe force microscopy and density functional theory, Phys. Rev. B 83 (2011) 235434.
[48] L. Liu, N.S. Xu, Y. Ke, H. Chen, Y. Zhang, S. Deng, Sensing by surface work function modulation: high performance gas Sensing using van der waals stacked bipolar junction transistor, Sens. Actuators B: Chem. 345 (2021) 130340.
[49] S. Khammuang, K. Wongphen, T. Hussain, K. Kotmool, Enhanced NH_3 and NO sensing performance of $Ti_3C_2O_2$ MXene by biaxial strain: insights from first-principles calculations, Phys. Chem. Chem. Phys. 27 (2025) 3827–3833.
[50] B.A. Kalwar, W. Fangzong, A.M. Soomro, M.R. Naich, M.H. Saeed, I. Ahmed, Highly sensitive work function type room temperature gas sensor based on Ti doped hBN monolayer for sensing CO_2, CO, H_2S, HF and NO. A DFT study, RSC Adv. 12 (2022) 34185–34199.